Macalester Journal of Physics and Astronomy

Volume 12
Issue 1 *Spring 2024*

Article 6

May 2024

Linking the Population of Binary Black Holes with the Stochastic Gravitational-Wave Background

Olivia X. Laske
Macalester College, olaske@macalester.edu

Follow this and additional works at: https://digitalcommons.macalester.edu/mjpa

Part of the Cosmology, Relativity, and Gravity Commons, and the Physics Commons

Recommended Citation
Laske, Olivia X. (2024) "Linking the Population of Binary Black Holes with the Stochastic Gravitational-Wave Background," *Macalester Journal of Physics and Astronomy*: Vol. 12: Iss. 1, Article 6.
Available at: https://digitalcommons.macalester.edu/mjpa/vol12/iss1/6

This Honors Project - Open Access is brought to you for free and open access by the Physics and Astronomy Department at DigitalCommons@Macalester College. It has been accepted for inclusion in Macalester Journal of Physics and Astronomy by an authorized editor of DigitalCommons@Macalester College. For more information, please contact scholarpub@macalester.edu.

Macalester College

Linking the Population of Binary Black Holes with the Stochastic Gravitational-Wave Background

Abstract

The astrophysical stochastic gravitational-wave background (SGWB) is the product of overlapping waveforms that create a single unresolvable background. While current LIGO sensitivity is insufficient to uncover the SGWB, future space-based detectors and Third Generation (3G) experiments are expected to probe deep enough for detection. Predictions of the SGWB can constrain future searches as well as provide insight into star formation, merger history, and mass distribution. Here, three primary methods are used to calculate a theoretical SGWB. The first method integrates over a precomputed mass distribution probability grid, while the second and third employ Monte Carlo integration with simulated data. After standardizing a prior distribution across both methods, the output energy density spectra is analyzed with regard to parameters such as binary black hole mass, merger rate, and spin distribution. Increasing the maximum merger mass shifts the gravitational-wave (GW) energy density peak to lower frequencies, while increasing merger rate parameters increases the GW energy density. In addition, higher spin magnitude and more closely aligned spins produce a maximum GW energy density higher in amplitude and frequency.

Keywords

gravitational waves, LIGO, stochastic gravitational-wave background, binary black holes

This honors project - open access is available in Macalester Journal of Physics and Astronomy: https://digitalcommons.macalester.edu/mjpa/vol12/iss1/6

MACALESTER COLLEGE

Linking the Population of Binary Black Holes with the Stochastic Gravitational-Wave Background

by

Olivia X. Laske

in the

Department of Physics and Astronomy

Advisors: John M. Cannon, Patrick M. Meyers, Arianna I. Renzini

April 29, 2024

MACALESTER COLLEGE

Abstract

Department of Physics and Astronomy

by Olivia X. Laske

The astrophysical stochastic gravitational-wave background (SGWB) is the product of overlapping waveforms that create a single unresolvable background. While current LIGO sensitivity is insufficient to uncover the SGWB, future space-based detectors and Third Generation (3G) experiments are expected to probe deep enough for detection. Predictions of the SGWB can constrain future searches as well as provide insight into star formation, merger history, and mass distribution. Here, three primary methods are used to calculate a theoretical SGWB. The first method integrates over a precomputed mass distribution probability grid, while the second and third employ Monte Carlo integration with simulated data. After standardizing a prior distribution across both methods, the output energy density spectra is analyzed with regard to parameters such as binary black hole mass, merger rate, and spin distribution. Increasing the maximum merger mass shifts the gravitational-wave (GW) energy density peak to lower frequencies, while increasing merger rate parameters increases the GW energy density. In addition, higher spin magnitude and more closely aligned spins produce a maximum GW energy density higher in amplitude and frequency.

Acknowledgements

This material is based upon work supported by the National Science Foundation. Any opinions, findings, and conclusions or recommendations expressed in this material are those of the author(s) and do not necessarily reflect the views of the National Science Foundation.

Thank you to the California Institute of Technology, the LIGO SURF program, LIGO Lab, and the National Science Foundation for making this research possible. Thank you to Alan Weinstein, director of the LIGO SURF program.

Thank you to Dr. Thomas Callister, Dr. Arianna Renzini, and Simona Miller for your code and advice, and to Pritvik Sinhadc for working on this project with me.

I would also like to thank Dr. Patrick Meyers for being a mentor to me during the past year. This project would not have been possible without your patience, support, and guidance. I appreciate your willingness to explain technical concepts to me and to walk me through each step of the project. I am incredibly grateful that I was able to extend my summer research at LIGO SURF with you throughout this academic year, and I am excited to see the next steps for this project.

Thank you to my physics advisor Dr. John Cannon. Taking Observational Astronomy with you was my first introduction to astronomy research and ultimately has led me to pursue a career in physics research. In addition, thank you for welcoming me into the MACRO (Macalester Augustana Coe Remote Observatory) Consortium and providing the incredible opportunity to visit the *Robert L. Mutel Telescope* (RLMT) in Sonoita, Arizona. I truly cannot express the amount of gratitude I have for your support and guidance throughout my years at Macalester.

I would like to extend a special thanks to my honors committee members, Dr. John Cannon, Dr. Anna Williams, and Dr. Michael Coughlin.

Finally, thank you to the Macalester Physics and Astronomy Department, friends and family for all of your support throughout my academic journey.

Contents

List of Figures

List of Tables

CHAPTER 1: Introduction

1.1 Overview

Gravitational waves (GWs) are perturbations in spacetime produced by highly energetic events. GWs were first observed in 2015 by the Laser Interferometer Gravitational-Wave Observatory (LIGO), located in Livingston, Louisiana and Hanford, Washington, with the detection of GW150914, a binary black hole merger (Abbott et al. 2016).

LIGO (Aasi et al. 2015) is joined by several other second generation (2G), ground-based GW observatories sensitive to frequencies in the 10-10000 Hz range, including Virgo in Italy (Acernese et al. 2015), GEO600 in Germany (Affeldt et al. 2014; Dooley et al. 2016; Luck et al. 2010), and the Kamioka Gravitational-Wave Detector (KAGRA) (Akutsu et al. 2020; Aso et al. 2013; Somiya 2012) in Japan. The LVK network is comprised of LIGO, Virgo, and KAGRA. See Abbott et al. (2020) for a summary of detector upgrades and a timeline of observation runs.

In addition, the space-based detector Laser Interferometer Space Antenna (LISA) (Babak et al. 2021), sensitive to $10^{-5} - 10^{-1}$ Hz, and Third Generation (3G) experiments Einstein Telescope (ET) (Hild et al. 2011; Punturo et al. 2010; Team 2020) and Cosmic Explorer (CE) (Abbott et al. 2017; Evans et al. 2021; Reitze et al. 2019), sensitive to 1-10000 Hz, are expected to launch in the 2030s.

For nanohertz frequencies, pulsar timing arrays include the North American Nanohertz Observatory for Gravitational Waves (NANOGrav), European Pulsar Timing Array (EPTA), and Parkes Pulsar Timing Array (PPTA), and the Indian Pulsar Timing Array Project (InPTA), which are collectively known as the International Pulsar Timing Array (IPTA).

LIGO and other 2G detectors take the form of a Michelson interferometer, in which an incident laser beam is split into orthogonal reflected and transmitted beam components along the two arms of the detector. The beams are subsequently reflected back toward the beam splitter and recombined. During a GW event, the arms of the detector are compressed and rarefied, causing the two beams to shift out of phase and form a detectable interference pattern.

GWs have plus (h_+) and cross ($h_\times$) polarizations. Assuming propagation is along the positive z axis, Figure 1.1 demonstrates the stretching and squeezing of spacetime as a polarized GW passes through a ring of particles. In the upper panel, the GW is plus-polarized, and spacetime is distorted in the x and y directions. In the lower panel, the GW is cross-polarized, and spacetime is distorted at an angle of $\pi/4$ to the x and y directions. Because GWs shift space in the plane perpendicular to the direction of propagation, the L shape of 2G detectors ensures that signals originating from any direction are observable.

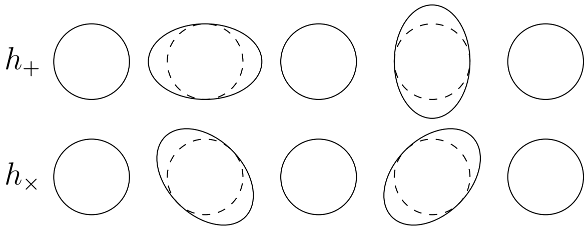

Figure 1.1: Plus (upper panel) and cross (lower panel) polarizations of gravitational waves.

The LVK network relies on either matched filtering or cross correlation to confirm GW signals, depending on the signal type. Matched filtering correlates a template waveform with the suspected signal and is typically used to confirm signals produced by compact binary coalescences. Cross correlation, on the other hand, correlates data between two detectors and is the primary method for detecting stochastic signals. The numerous noise sources, ranging from the seismic noise of ocean waves and earthquakes to the thermal noise of suspension mirror resonance frequencies, prove difficult to distinguish from GW signals, especially as the strain produced by GWs is on the order of 10^{-21} (Abbott et al. 2016). Ensuring signal presence at multiple interferometers both reliably confirms GW signals and allows for more accurate sky localization.

GW signals are often categorized into continuous, compact binary inspiral, burst, and stochastic types. Continuous GWs are produced by large, rotating systems, such as neutron stars, and appear as a sinusoidal pattern of detector strain over long periods of time (Piccinni 2022). Compact binary inspirals arise from mergers of dense objects, such as black holes and neutron stars, and are characterized by a chirp signal in time-frequency space (Bustillo et al. 2020). Through O3, LIGO has detected 90 GW events stemming from compact binary inspirals (Piccinni 2022). Burst GW sources include Type II supernovae and are measured on short time scales (Abbott et al. 2019). Finally, stochastic signals are the sum of numerous unresolved GW sources that form a background (Renzini et al. 2022). LIGO has yet to detect continuous, burst, and stochastic signals.

1.2 The Stochastic Gravitational-Wave Background

The stochastic gravitational-wave background (SGWB) is of particular interest, especially as the involved GWs can originate from the very early Universe, not long after the Big Bang. Because the Universe at the time was opaque to photons, the SGWB is one of the only means of studying this era. In addition, understanding the effect of the binary black hole (BBH) population on the SGWB can be used to constrain properties such as merger rate and mass distribution (Callister et al. 2020, 2016; Turbang et al. 2023).

The SGWB is often divided into two categories: cosmological and astrophysical. Cosmological sources include events that occurred in the early Universe, such as inflation, during which rapid expansion drove GWs into an isotropic background. Astrophysical sources are comprised of individual events such as mergers and pulsars. Figure 1.2 from Renzini et al. (2022) depicts the predicted SGWBs for several cosmological and astrophysical sources across the frequency spectrum. Each solid color represents a different source of GWs. The brown curve originates from supermassive binary black holes (SMBBH), the pink curve from cosmic strings, the gray curve from first-order phase transitions (FOPTs), the yellow curve from stellar-mass compact binary coalescences (CBCs), and the blue curve from inflation. The frequency sensitivity of the LVK network ranges from 10 Hz to 10 kHz (Martynov et al. 2016), which encapsulates the predicted SGWB arising from CBCs. The SGWB from supermassive binary black holes (SMBBHs) lies outside of this range from 10^{-10} Hz to 10^{-7} Hz. This project specifically focuses on stellar-mass BBHs

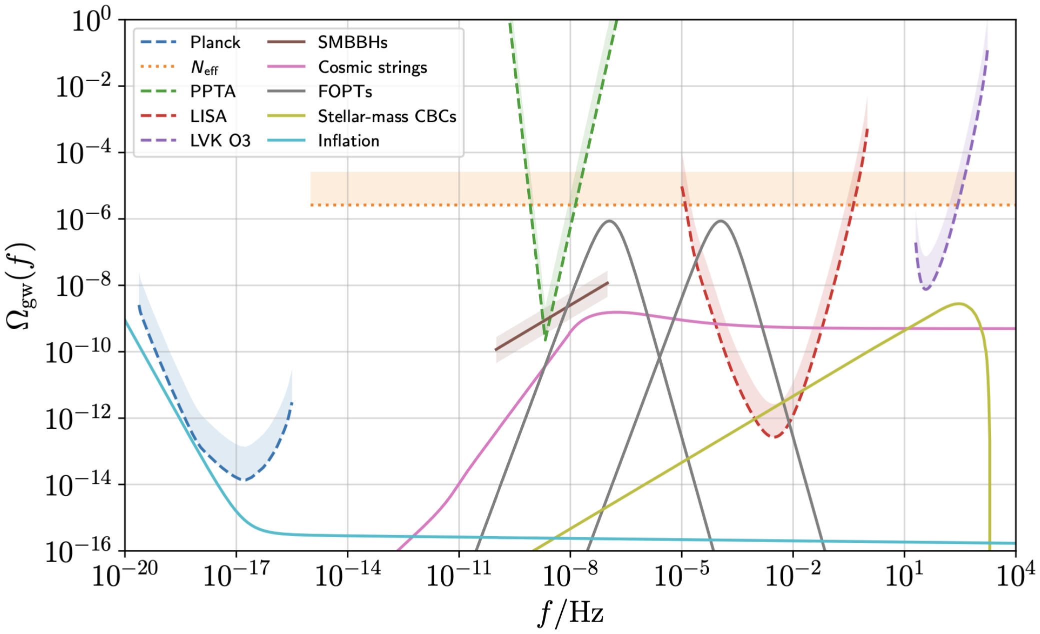

FIGURE 1.2: Predicted GW backgrounds from different sources across the frequency spectrum. The dotted curves represent detector sensitivity curves, while the solid curves are stochastic background predictions for different sources. The shaded regions are error bounds on the curves. Figure from Renzini et al. (2022).

(1 to 100 $M_\odot$), which are expected to be the majority of the BBH signals that contribute to SGWB in the LVK frequency range.

The first two dashed lines in Figure 1.2 represent observational constraints, and the three last dashed lines represent the sensitivity curves for different detectors. The dashed green curve corresponds to the Parkes Pulsar Timing Array (PPTA), the dashed red curve to the Laser Interferometer Space Antenna (LISA), and the dashed purple curve to the LVK (LIGO-Virgo-KAGRA) network. Note that the PPTA curve intersects the predicted background for SMBBHs, which is consistent with recent evidence for a SGWB at nanohertz frequencies (Agazie et al. 2023; EPTA Collaboration et al. 2023; Reardon et al. 2023; Xu et al. 2023). The dashed red curve, on the other hand, is for the Laser Interferometer Space Antenna (LISA). The overlap with the yellow curve predicts that LISA could uncover the SGWB originating from cosmic strings, FOPTs, and stellar-mass CBCs.

Detector sensitivity and resolution limits result in unresolved GW signals, which overlap to create a measurable SGWB. With current detector sensitivity in the

LVK frequency band, though, the SGWB is undetectable, as illustrated in Figure 1.3. The orange bounds predict the combined SGWB from BBHs, BNSs, and NSBHs. The solid black, dashed, and dot-dashed curves are 1-sigma power-law integrated sensitivity curves assuming 1 year of observation for the O3, Design HLV, and Design A+ observing runs, respectively (Thrane & Romano 2013). While the O3 and Design HLV curves do not intersect the total background bounds, Design A+ LIGO, as well as detectors LISA, ET, and CE, will begin to probe the sensitivities required to detect the SGWB from unresolved compact binary mergers.

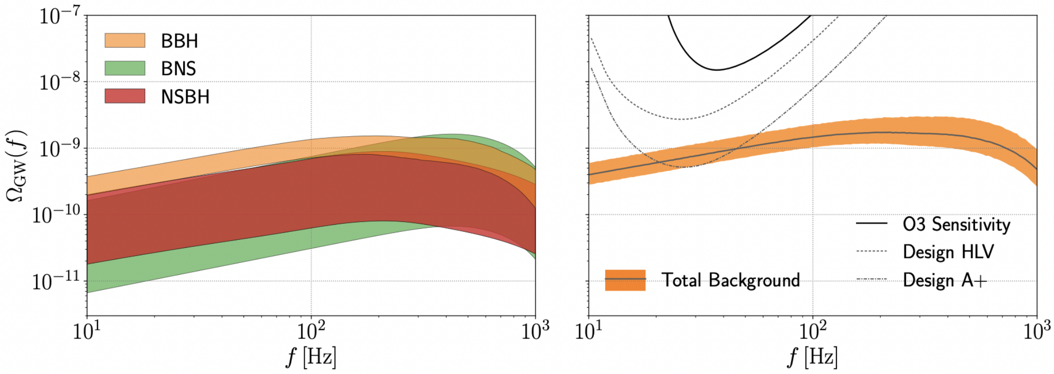

FIGURE 1.3: Current detector limits with regard to the SGWB. The left panel depicts the breakdown of the astrophysical stochastic background at LVK frequencies into BBH, BNS, and NSBH components. The right panel compares the combined background from BBHs, BNSs, and NSBHs with the sensitivity curves for the O3, O4, and O5 LIGO observing runs. Figure from Renzini et al. (2022).

Detectors must be sufficiently far apart in order to ensure that they are not receiving identical noise sources. However, one consequence of physically distant detectors is the overlap reduction function $\Gamma(f)$ (ORF), shown for the LVK network in Figure 1.4. The overlap reduction function is related to the correlation between the two detectors:

$$\langle h_1(f) h_2(f) \rangle = T_{\mathrm{obs}} \Gamma(f) H(f), \tag{1.1}$$

where $h_1(f)$ and $h_2(f)$ are the GW signals from detectors 1 and 2, respectively, T_{obs} is the duration of observation time, and $H(f)$ is the power spectrum of all GWs in units of strain squared divided by Hertz. A value of $|\Gamma(f)| = 1$ occurs when the measured power is equal to the GW power after cross-correlating data.

A value of $|\Gamma(f)| < 1$, however, occurs when the measured power is less than the GW power, signifying reduced sensitivity.

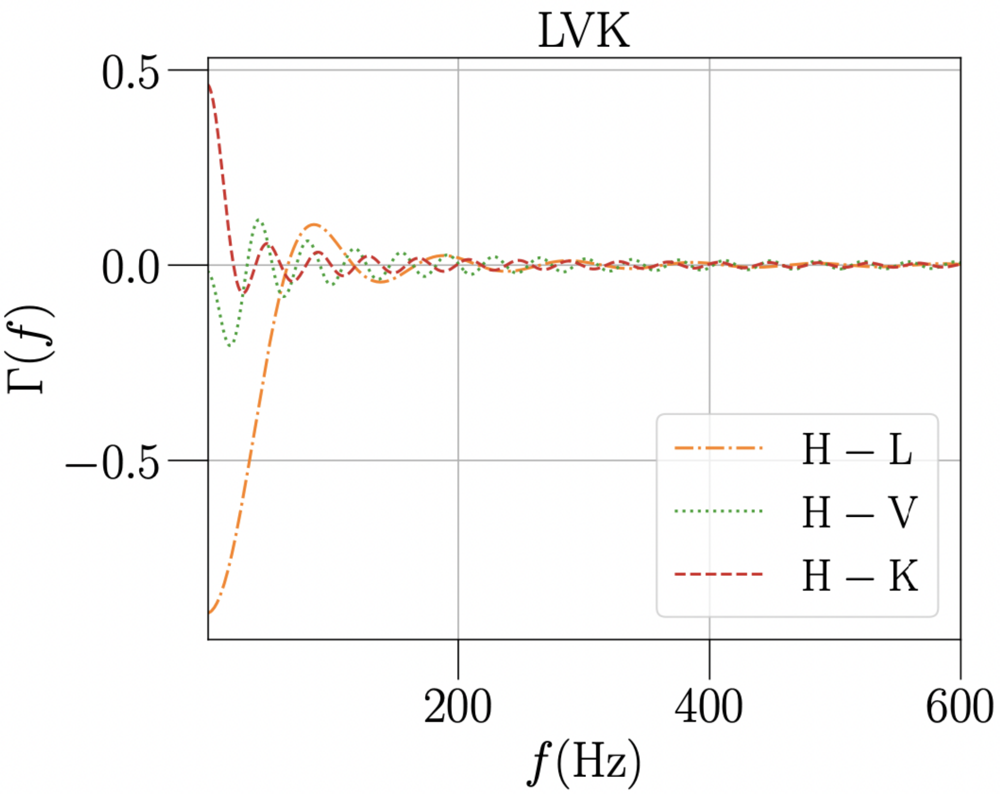

FIGURE 1.4: Overlap reduction function for the LVK network. Figure from Renzini et al. (2022).

An oscillating GW signal is time-shifted between the detectors, which reduces signal correlation between them. A consequence of time-shifted signals is that the magnitude of the overlap reduction function is greatest at lower frequencies, then rapidly dampens with increasing frequency.

For detectors that are further apart, such as LIGO Hanford and Virgo, $|\Gamma(f)|$ is decays more quickly. In addition, $|\Gamma(0)|$ decreases as detector separation increases. As a result, assuming a uniform, isotropic, unpolarized, and Gaussian SGWB, LIGO is more sensitive to low-frequencies, where the wavelength is significantly greater than the distance between the detectors.

Furthermore, the detectors are not optimally oriented, which causes $|\Gamma(f)|$ to decrease. Detectors that are either parallel or antiparallel maximize signal correlation by ensuring that strain amplitude is identical between the sites. Detectors oriented 45 degrees, on the other hand, produce an ORF of 0, meaning that their data is uncorrelated. LIGO Hanford and LIGO Livingston are positioned nearly antiparallel. As a result, the ORF is very close to -1, as seen by the dash-dotted orange curve in Figure 1.4. The data from LIGO Hanford and Advanced Virgo has very little correlation, and the ORF is much closer to 0, as shown by the dotted green curve.

CHAPTER 2: Methods

Several different methods may be used to calculate the SGWB originating from binary black holes. The first method, developed by Thomas Callister (hereby referred to as the Gridded Method) and used in Abbott et al. (2021) and Abbott et al. (2023), uses a predefined mass distribution to create a grid of (m_1, q) points, converts them to $(\ln M_{\rm tot}, q)$ space with the Jacobian, and calculates the spectral energy density at each grid point. The second method, developed in C by Tania Regimbau and rewritten in Python by Arianna Renzini (the Monte Carlo Method), generates a frequency domain waveform and calculates the power spectral density for each injection in a list of injections. The final method (Weighted Method) precalculates the spectral energy density for a reference set of priors then reweights each value to match a specified distribution on CBC parameters.

While each of the methods produce similar SGWB predictions, some methods are advantageous over others depending on the usage. For instance, the Gridded Method produces identical spectra for each calculation if no parameters are changed. On the other hand, Monte Carlo based methods, including the Monte Carlo and Weighted Methods, permit a more realistic output energy density with confidence intervals. The Weighted Method is particularly useful when quick calculation is needed. As a result, in this section, we compare the SGWB predictions from each of these four methods and examine how certain methods may be advantageous over others depending on the usage. In the next section, we then employ the Gridded and Monte Carlo Methods to analyze the effect of black hole population properties on the SGWB.

2.1 Theoretical Calculation of the SGWB

The GW energy density can be written as follows:

$$\Omega_{\mathrm{GW}}(f) = \frac{1}{\rho_{\mathrm{c}}} \int_0^\infty dz \frac{N(z)}{1+z} \left[f_{\mathrm{r}} \frac{dE_{\mathrm{GW}}}{df_{\mathrm{r}}} \right]_{f_{\mathrm{r}}=f(1+z)}, \tag{2.1}$$

$$\rho_{\mathrm{c}} = \frac{3H_0^2 c^2}{8\pi G}, \tag{2.2}$$

where ρ_c is the critical energy density for a flat universe, $N(z)$ is number of GW sources as a function of redshift, z is redshift, $dE_{\mathrm{GW}}/df_{\mathrm{r}}$ is spectral energy density, f_{r} is rest frame frequency, $H_0 = 67.4$ km s^{-1} Mpc^{-1} is the Hubble constant (see Appendix A), $c = 2.99792458 \cdot 10^8$ m s^{-1} is the speed of light, and $G = 6.6743015 \cdot 10^{-11}$ m^3 kg^{-1} s^{-2} is the universal gravitational constant. The integral of Equation 2.1 encompasses the entirety of redshift history. One interpretation of Equation 2.1 is that the components inside the integral multiply $N(z)$ by the spectral energy density weighted by f. At $z = 0$, $f_{\mathrm{r}} = f$, and $\Omega_{\mathrm{GW}}(f) = f(N_0/\rho_{\mathrm{c}})(dE_{\mathrm{GW}}/df)$, demonstrating that Ω_{GW} is proportional to $N(z)$.

Fractional energy density can be averaged over source parameters θ, which include black hole component masses m_1 and m_2, component spins χ_1 and χ_2, and redshift z. The black hole with the greater mass is described by mass m_1 and spin χ_1, while the black hole with the lesser mass is described by mass m_2 and spin χ_2. The component masses may range from approximately 5 $M_\odot$ to 50 $M_\odot$ (Abbott et al. 2023), and the component spin magnitudes are from 0 to 1. Redshift is caused by non-zero velocity away from an observer and is equal to the change in observed wavelength divided by the true wavelength such that $z = \Delta\lambda/\lambda$. Due to the accelerating expansion of the Universe, redshift can also be used as a measure of when an event occurred, with increasing redshift corresponding to earlier in time.

Since each binary black hole merger is associated with the set of source parameters θ, the fractional energy density can be determined by integrating over source parameter probability distribution $p(\theta)$ multiplied by the spectral energy density $dE_{\mathrm{GW}}(\theta; f_{\mathrm{r}})/df_{\mathrm{r}}$ using parameter set θ. The integration variable is θ, meaning that the integration considers all plausible parameter combinations and incorporates the comprehensive list of binary black hole mergers into the SGWB calculation.

More specifically, $p(\theta)$ describes the population of binary black holes and encompasses the probability distributions on black hole source parameters θ. As the initial assumed probability distribution, $p(\theta)$ is also known as a prior distribution. We later sample parameters from $p(\theta)$ to generate injections of binary black hole mergers. The prior distributions on each parameter are written in the Python package `bilby`, which provides functions to create and sample from customizable priors (Ashton et al. 2019).

The number of GW sources $N(z)$ can be rewritten in terms of event rate, redshift, and the Hubble parameter. Therefore, Equation 2.1 becomes the following after removing f from the integral:

$$\Omega_{\rm GW}(f) = \frac{f}{\rho_{\rm c}} \int_0^{z_{\rm max}} dz \frac{\mathcal{R}(z)}{(1+z)H(z)} \left\langle \frac{dE_{\rm GW}}{df_{\rm r}} \bigg|_{f_{\rm r}=f(1+z)} \right\rangle, \tag{2.3}$$

$$\left\langle \frac{dE_{\rm GW}}{df_{\rm r}} \right\rangle = \int d\theta p(\theta) \frac{dE_{\rm GW}(\theta; f_{\rm r})}{df_{\rm r}}, \tag{2.4}$$

where $z_{\rm max}$ is the maximum redshift for a BBH, $\mathcal{R}(z) = dN(z)/dt$ is the BBH merger rate, and $H(z)$ is the Hubble parameter as a function of redshift (see Appendix A).

Multiple methods are commonly used to evaluate Equation 2.3, such as the Gridded, Monte Carlo, and Weighted Methods. The Gridded Method approximates the integral as a Riemann sum across redshift history, whereas the other two methods sum over a list of sampled events.

Regardless of the method, the frequency of the compact binary coalescence inspirals $dE_{\rm GW}/df_{\rm r}$ is proportional to $f^{-1/3}$ (see Equation 2.16). Multiplying by f to obtain the energy contribution from each event yields $\Omega_{\rm GW} \propto f^{2/3}$. As a result, the SGWB can be modeled by a power law of the following form (Callister et al. 2016; Renzini et al. 2022):

$$\Omega_{\rm GW}(f) = \Omega_{GW}(f_{\rm ref}) \left(\frac{f}{f_{\rm ref}}\right)^{\alpha}, \tag{2.5}$$

where $\Omega_{\mathrm{GW}}(f)$ is dimensionless GW energy density, f is frequency, and α is the spectral index of the signal.

2.2 Standard Prior Dictionary

In order to ensure that parameters remain consistent across all methods, a set of standard `bilby` priors is defined as in Table 2.1 (Ashton et al. 2019). `mass_1` (m_1) is the greater component mass, `mass_ratio` (q) is defined as $q = m_2/m_1$, `theta_jn` (θ_{jn}) is the inclination angle of the merger, `a_1` (χ_1) and `a_2` (χ_2) are the component spin magnitudes, `phi_12` (ϕ_{12}) is the azimuthal angle between the component spins around the orbital angular momentum, `phi_jl` (ϕ_{jl}) is the angle between the total anglular momentum and the line of sight, `redshift` (z) is the redshift of the merger, and `geocent_time` (t_{geo}) is the elapsed geocentric time after the start of the observation period (T_{obs}) before the merger. Figure 2.1 from Biscoveanu et al. (2021) displays a visual representation of θ_{jn}, ϕ_{12}, and ϕ_{jl}. The prior probabilities on `mass_1` and `mass_ratio`, $p(m_1)$ and $p(q)$, are a power law, while `theta_jn` and `geocent_time` are uniform.

Parameter	Prior	Hyperparameters
`mass_1`	Power Law	$\alpha = -2.8$
`mass_ratio`	Power Law	$\alpha = 1.5$
`theta_jn`	Uniform	min = 0, max = 2π
`a_1`	0	0
`a_2`	0	0
`phi_12`	Uniform	min = 0, max = 2π
`phi_jl`	Uniform	min = 0, max = 2π
`redshift`	$\propto \frac{1}{1+z}\mathcal{R}(z)\frac{dV_c}{dz}$	min = 0, max = 10
`geocent_time`	Uniform	min = 0, max = T_{obs}

TABLE 2.1: Standard set of priors.

The redshift probability distribution `redshift` is defined in Equation 2.6 from Callister et al. (2020). The distribution depends on the merger rate and comoving volume per unit redshift, with the term $(1+z)^{-1}$ converting from source frame to detector frame:

$$p(z) \propto \frac{1}{1+z}\mathcal{R}(z)\frac{dV_c}{dz}. \tag{2.6}$$

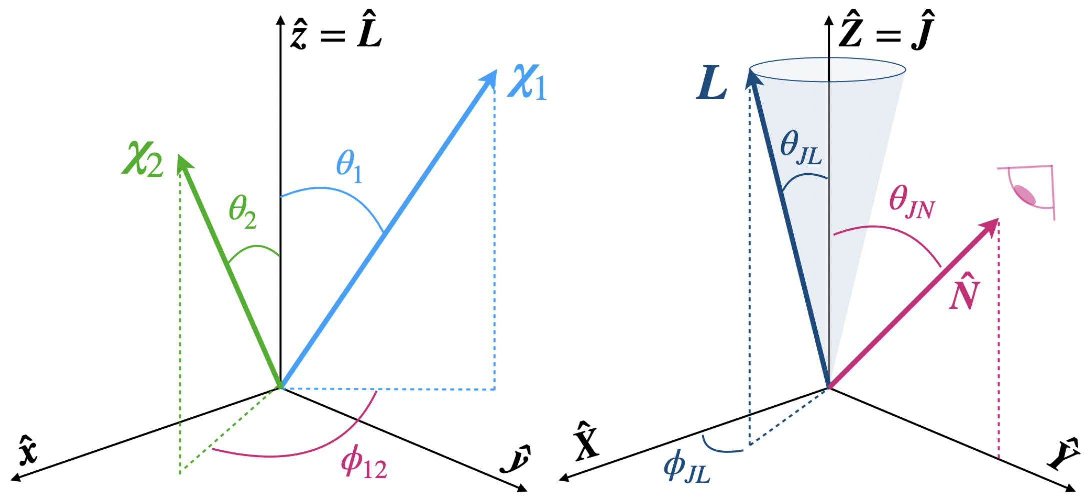

FIGURE 2.1: Diagram of spin angles, including θ_{jn}, ϕ_{12}, and ϕ_{jl}. θ_{JN} is the angle between the line of sight $\hat{N}$ and the total angular momentum $\hat{J}$. ϕ_{12} is the azimuthal angle between the spin vectors of the two black holes projected into the orbital plane. ϕ_{JL} is the azimuthal angle between the $\hat{X}$ axis and the projection of the orbital angular momentum onto the $\hat{X} - \hat{Y}$ plane, where the $\hat{Z}$ axis is the direction of the total angular momentum. Figure from Biscoveanu et al. (2021).

The BBH merger rate $\mathcal{R}(z)$ is often modelled as follows:

$$\mathcal{R}(z) = \mathcal{C}(\alpha, \beta, z_{\mathrm{p}}) \frac{\mathcal{R}_0 (1+z)^{\alpha}}{1 + (\frac{1+z}{1+z_{\mathrm{p}}})^{\alpha+\beta}}, \tag{2.7}$$

$$\mathcal{C}(\alpha, \beta, z_{\mathrm{p}}) = 1 + (1 + z_{\mathrm{p}})^{-(\alpha+\beta)}, \tag{2.8}$$

where $\mathcal{R}_0$ is the current merger rate and $\mathcal{C}(\alpha, \beta, z_{\mathrm{p}})$ is a normalization constant to satisfy the boundary condition $\mathcal{R}(0) = \mathcal{R}_0$. Values α and β shape the growth and decay of $\mathcal{R}(z)$ (Callister et al. 2020):

$$\frac{d\mathcal{R}(z < z_{\mathrm{p}})}{dz} \propto (1+z)^{\alpha}, \tag{2.9}$$

$$\frac{d\mathcal{R}(z > z_{\mathrm{p}})}{dz} \propto (1+z)^{-\beta}. \tag{2.10}$$

Figure 2.2 depicts the normalized redshift probability distribution for $\alpha = 1.9$, $\beta = 3.4$, $z_{\mathrm{p}} = 2.4$, and $\mathcal{R}_0 = 28.3$ Gpc^{-3} yr^{-1}, as in Callister et al. (2020). The peak in the graph represents cosmic noon, after which the rate of BBHs rapidly declines.

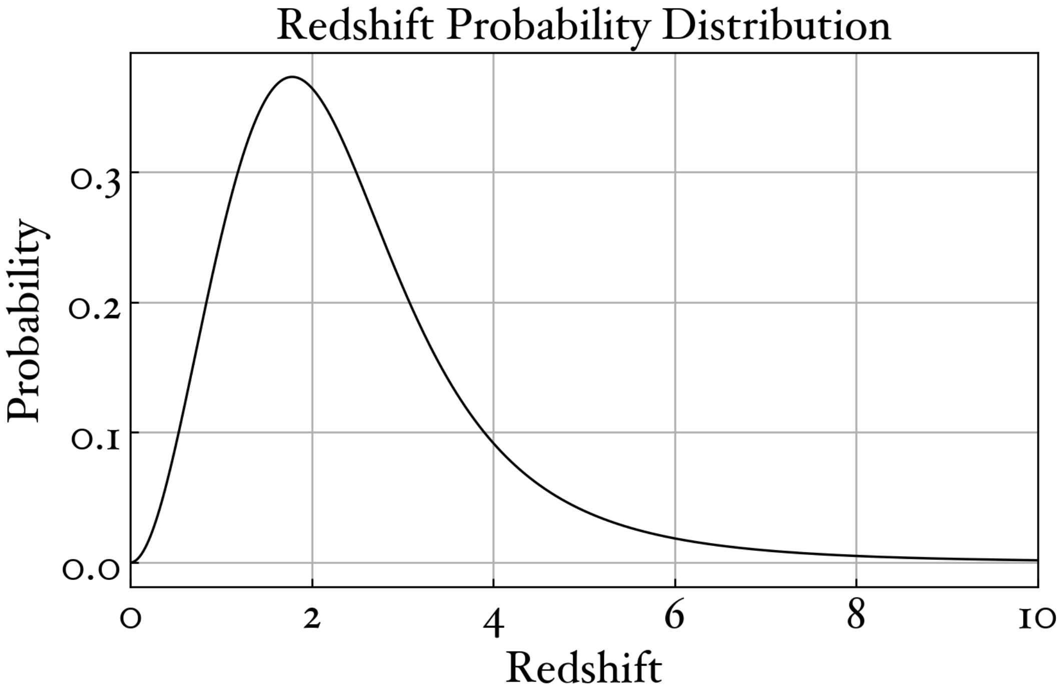

FIGURE 2.2: Redshift probability distribution using $\alpha = 1.9$, $\beta = 3.4$, $z_\mathrm{p} = 2.4$, and $\mathcal{R}_0 = 28.3$ Gpc^{-3} yr^{-1}.

2.3 Calculation of the SGWB with the Gridded Method

The Gridded Method converts the integral in Equation 2.3 into a Riemann sum:

$$\Omega_\mathrm{GW}(f) = \frac{f}{\rho_\mathrm{c}} \sum_{z=0}^{z_\mathrm{max}} \Delta z \frac{\mathcal{R}(z)}{(1+z)H(z)} \left\langle \frac{dE_\mathrm{GW}}{df_\mathrm{r}} \bigg|_{f_\mathrm{r}=f(1+z)} \right\rangle . \tag{2.11}$$

Since the maximum redshift of a binary black hole is equal to $z_\mathrm{max} = 10$, redshift bins are set from $z = 0$ to $z = 10$ with arbitrarily small steps $\Delta z = 0.01$. The spectral energy density, the term inside the angle brackets in Equation 2.11, is dependent on the BBH chirp mass (see Equations 2.14 and 2.15). As a result, we can spread out dE/df into a grid in (m_1, q) space with an associated mass distribution. Calculating the average spectral energy density then requires integrating over the grid. The average spectral energy density is weighted by the number of events, summed over redshift history, and multiplied by $f/\rho_{\rm c}$ to obtain the final GW energy density.

The Gridded Method can be broken down into four distinct steps:

1. Define the local merger rate.
2. Calculate the merger rate.
3. Determine the mass distribution probability grid.
4. Calculate the GW energy density $\Omega_{\rm GW}$.

The local merger rate describes the merger rate, which is the total number of mergers that occur per cubic Gpc per year, at $z = 0$. A BBH local merger rate is defined for subsequent merger rate density normalization such that $\mathcal{R}(z)_{\rm norm} = \mathcal{R}_0(\mathcal{R}(z)/\mathcal{R}(0))$. The Gridded Method uses $\mathcal{R}_0 = 28.3$ Gpc^{-3} yr^{-1}, which is the Power Law + Peak BBH merger rate ($z = 0.2$) from Abbott et al. (2023).

The local merger rate is used to find the merger rate, which is calculated from Equations 2.7 and 2.8 for each redshift bin, inputting $\alpha = 1.9$, $\beta = 3.4$, $z_{\rm p} = 2.4$, and $\mathcal{R}_0 = 28.3$ Gpc^{-3} yr^{-1}. Because the redshift prior (see Table 2.1) uses an identical model and redshift bins, the array of merger rates directly maps to the array of redshift probabilities, allowing us to find the merger rate probability as a function of redshift. Figure 2.3 displays a plot of the merger rate as a function of redshift.

The minimum and maximum BH masses are set such that $m_{\rm min} = 5$ M$_\odot$ and $m_{\rm max} = 50$ M$_\odot$. A probability grid of the mass distribution is defined in (m_1, q) space by evaluating $p(m_1)$ and $p(q)$ from their prior distributions defined in 2.1. The probabilities are then converted to $(\ln M_{\rm tot}, q)$ space with the Jacobian and normalized. Callister (2021) provides a table of Jacobians that converts between mass parameter pairs.

$$\frac{dP}{d\ln M_{\rm tot} dq} = \frac{dP}{dm_1 dq} \frac{M_{\rm tot}}{(1+q)}. \tag{2.12}$$

While the mass distribution was defined in (m_1, q) space here, the priors may be defined in terms of other mass parameter pairs as well. For instance, if the standard

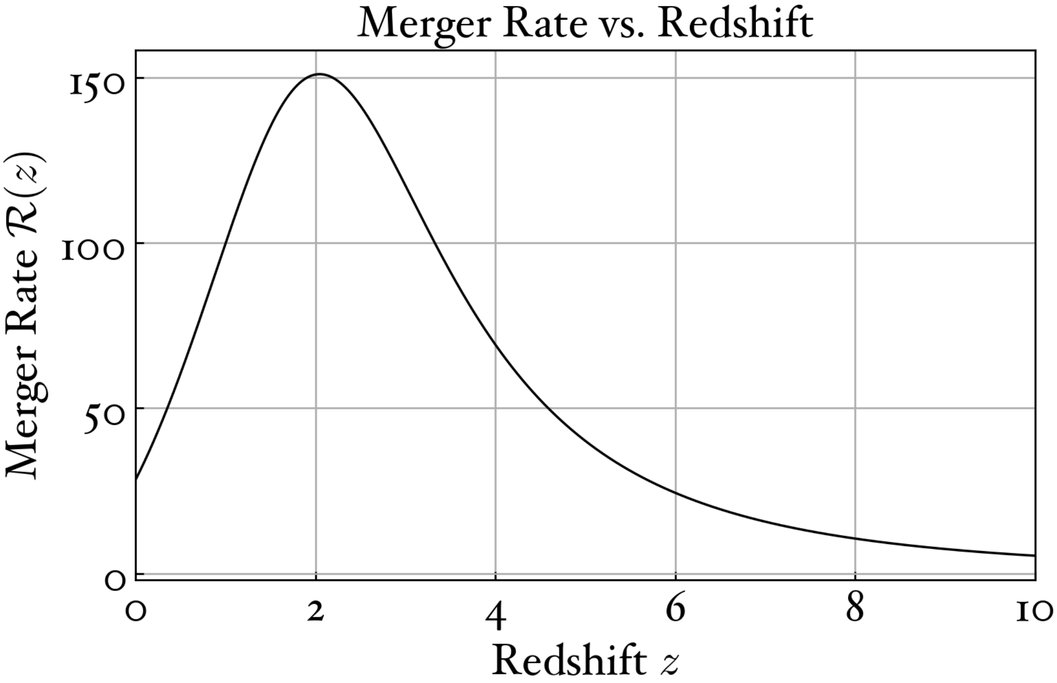

FIGURE 2.3: Merger rate using $\alpha = 1.9$, $\beta = 3.4$, $z_\text{p} = 2.4$, and $\mathcal{R}_0 = 28.3$ Gpc^{-3} yr^{-1}. The growth of $R(z)$ for $z < z_\text{p}$ is proportional to $(1+z)^{\alpha}$, and the decay of $R(z)$ for $z > z_\text{p}$ is proportional to $(1+z)^{-\beta}$. The parameter z_p controls the redshift at which the peak of $R(z)$ occurs. $\mathcal{R}_0$ is equal to the BBH merger rate at $z = 0$.

priors were alternatively defined in (m_1, m_2) space, Equation 2.12 is revised to the following:

$$\frac{dP}{d\ln M_\text{tot} dq} = \frac{dP}{dm_1 dm_2}\frac{M_\text{tot}^2}{(1+q)^2}. \tag{2.13}$$

Once the mass distribution probability grid has been determined, the spectral energy density can be calculated. For inspiralling compact binary systems, the spectral energy density $dE_{\mathrm{GW}}/df_{\mathrm{r}}$ is found as follows:

$$\frac{dE_{\mathrm{GW}}}{df} = \frac{(G\pi)^{2/3}\mathcal{M}^{5/3}}{3}H(f), \tag{2.14}$$

$$\mathcal{M} = \frac{(m_1 m_2)^{3/5}}{(m_1+m_2)^{1/5}}, \tag{2.15}$$

$$H(f) = \begin{cases} f^{-1/3} & (f < f_{\mathrm{merge}}) \\ \frac{f^{2/3}}{f_{\mathrm{merge}}} & (f_{\mathrm{merge}} \leq f < f_{\mathrm{ring}}) \\ \frac{1}{f_{\mathrm{merge}} f_{\mathrm{ring}}^{4/3}} \left(\frac{f}{1+(\frac{f-f_{\mathrm{ring}}}{\sigma/2})^2} \right)^2 & (f_{\mathrm{ring}} \leq f < f_{\mathrm{cutoff}}) \\ 0 & (f \geq f_{\mathrm{cutoff}}) \end{cases}. \tag{2.16}$$

Here, $\mathcal{M}$ is chirp mass, m_1 and m_2 are component masses, f is frequency, f_{merge} is the merger frequency, f_{ring} is the ringdown frequency, f_{cutoff} is the cutoff frequency, and σ is the width of the Lorentzian function around f_{ring} (Callister et al. 2016). Parameters f_{merge}, f_{ring}, f_{cutoff}, and σ are given by Table I in Ajith et al. (2008).

$H(f)$ can be understood as the spectral shape of the GW energy density. Figure 2.4 depicts $H(f)$ for varying values of $M_{\mathrm{tot}} = m_1 + m_2$ and z.

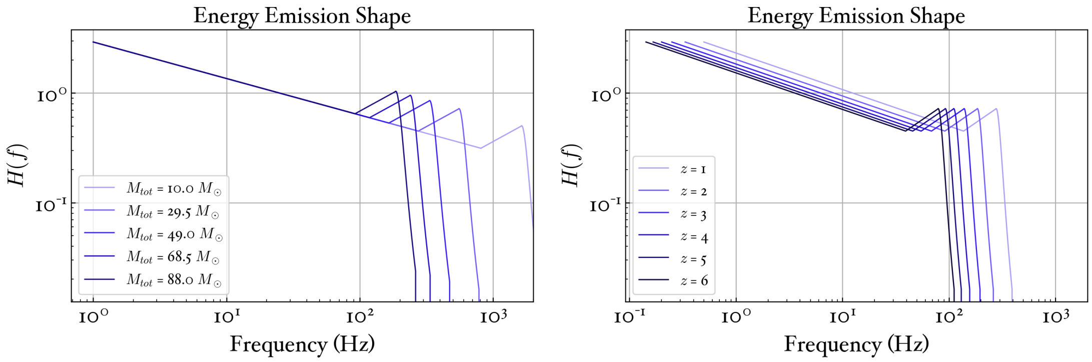

FIGURE 2.4: Spectral shape of GW energy density for varying values of $M_{\mathrm{tot}} = m_1 + m_2$ and z.

The left panel displays the shifting of $H(f)$ to lower frequencies and higher magnitudes as total mass increases, which confirms that more massive systems merge at lower frequencies with greater energy. The right panel demonstrates that higher redshifts push $H(f)$ to lower frequencies and magnitudes, as expected. As redshift increases, signals both become fainter and decrease in frequency.

Probability $p(\theta)$ in Equation 2.4 is given for (m_1, q) by $p(m_1)$ and $p(q)$, which was used to define the mass distribution probability grid. The chirp mass $\mathcal{M}$ can calculated from m_1 and $m_2 = m_1 q$. Integrating over each grid point accounts for all mass combinations of BBHs at redshift z, which is equivalent to the average spectral energy density. The merger rates and average spectral energy density are then inserted into Equation 2.3 to obtain the final GW energy density.

2.4 Calculation of the SGWB with the Monte Carlo Method

The Monte Carlo Method begins by sampling the priors given in Table 2.1. The resulting injections are inserted into the `Simulator` module of the Python library `pygwb` (Python-based library for gravitational-wave background searches), which generates an IMRPhenomXPHM waveform for each injection (Khan et al. 2019). The module then calculates Ω_{GW} by summing the spectral energy density of each event (Renzini et al. 2023):

$$\frac{dE}{df} = |h_+|^2 + |h_\times|^2, \tag{2.17}$$

where h_+ is the plus polarization, and $h_\times$ is the cross polarization. The GW energy density is then calculated with the following equation:

$$\Omega_{\mathrm{GW}}(f) = \frac{2}{T_{\mathrm{obs}}} \sum_{0}^{N} \frac{2\pi^2 f^3}{3H_0^2} \frac{dE}{df}, \tag{2.18}$$

where T_{obs} is the duration of observation time, and N is the number of sampled events. N is given by Callister et al. (2020):

$$N(\alpha, \beta, z_{\mathrm{p}}, \mathcal{R}_0) = T_{\mathrm{obs}} \int_0^{z_{\max}} dz \frac{1}{1+z} \mathcal{R}(\alpha, \beta, z_{\mathrm{p}}, \mathcal{R}_0; z) \frac{dV_{\mathrm{c}}}{dz}. \tag{2.19}$$

After computing a theoretical value for N, the number of injections is determined with a Poisson process with the expected number of events given by Equation 2.19 (see Appendix B).

In order to sample enough events to minimize uncertainty in the SGWB, the observing time should be maximized. However, sampling events requires simulating N waveforms over T_{obs}, which uses significant run time. Instead of increasing T_{obs} to output Nn injections, where n is an integer, we can incorporate the simulated data for Nn injections by averaging Ω_{GW} over n iterations. In other words, this technique has the same effect as increasing T_{obs}. Because T_{obs} is lower when averaging over n iterations, less strain data is simulated for each iteration. As a result, the process is quicker, despite the number of injections remaining constant. Note that the number of injections in each iteration still uses a Poisson process to account for statistical uncertainty in the number of events.

2.5 Calculation of the SGWB with the Weighted Method

The Weighted Method follows the same steps as the Monte Carlo Method to calculate a reference spectral energy density (see Equation 2.17). We use a set of reference priors uniform in `mass_1`, `mass_ratio`, `theta_jn`, `phi_12`, `phi_jl`, `redshift`, and `geocent_time`, with `a_1` and `a_2` set to 0. In order to determine the spectral energy density for the priors in Table 2.1, as opposed to the reference priors, each reference spectral energy density is reweighted according to the following equation, given by Turbang et al. (2023):

$$w_i = \frac{p(z^i)}{p_{\text{draw}}(z^i)} \frac{p(m_1^i)}{p_{\text{draw}}(m_1^i)} \frac{p(q^i)}{p_{\text{draw}}(q^i)}, \tag{2.20}$$

where w_i is the weight for an injection i, p are the probabilities of a draw taken from the desired priors, and p_{draw} are the probabilities of a draw taken from the reference priors. In effect, Equation 2.20 is weighting the reference prior distribution to match the desired distribution.

The weighted spectral energy densities for each waveform are summed to determine Ω_{GW} for the new priors (Turbang et al. 2023):

$$\Omega_{\mathrm{GW}}(f) = \mathcal{R}\frac{2\pi^2 f^3}{3H_0^2}\frac{1}{N}\sum_{i=1}^{N} w_i \left(\frac{dE}{df}\right)_{\mathrm{ref},i} . \tag{2.21}$$

The Weighted Method is especially useful when analyzing the effect of different parameters on the SGWB. Finding a predicted GW energy density for n values of a parameter using the Gridded Method or Monte Carlo Methods requires calculating the average spectral energy density n times, which takes a significant amount of run time. The Weighted Method, on the other hand, stores the reference spectral energy density in memory during the precalculation step. As a result, dE/df only needs to be computed once. Varying parameters then only requires a new weighting scheme, which is a quick calculation. Therefore, both the total number of calculations and the run time are significantly reduced.

CHAPTER 3: Results

The following section details the energy density spectra generated by each of the methods. The Gridded Method is used to explore the dependence of the SGWB on varying parameters.

Monte Carlo sampling in both the Monte Carlo and Weighted Methods causes the output energy density spectrum to differ between each run. Because the Gridded Method produces static results, changes in the energy density spectrum highlight the effect of altered parameters. The Monte Carlo Method, on the other hand, is used to analyze the effect of spin on the SGWB in Section 3.3 because of the allowance of spin priors in `bilby`. Perhaps most importantly, the Monte Carlo Method requires significantly less calculations, allowing for increased numbers of parameters and trial runs.

3.1 Comparison of Methods

Figure 3.1 displays the spectra generated by all three methods. The black curve shows the output from the Gridded Method, the red curve from the Monte Carlo Method, and the green curve from the Weighted method, with the highlighted regions representing the 5th and 95th percentiles. Ideally, all three curves are identical. However, each of the methods generates the same spectral shape for low frequencies, but they increasingly deviate frequencies above ≈ 100 Hz. The Gridded Method is generally consistent with the 2/3 power law at low frequencies 3.2. However, as shown in Figures 3.3 and 3.4, the Monte Carlo and Weighted Methods have noticeable discrepancies with the energy density curve more closely matching a 1/2 power law. As a result, we conclude that the deviation from the predicted 2/3 power law is due to additional complexities in the inspiral phase of BBHs revealed when using a more realistic waveform model.

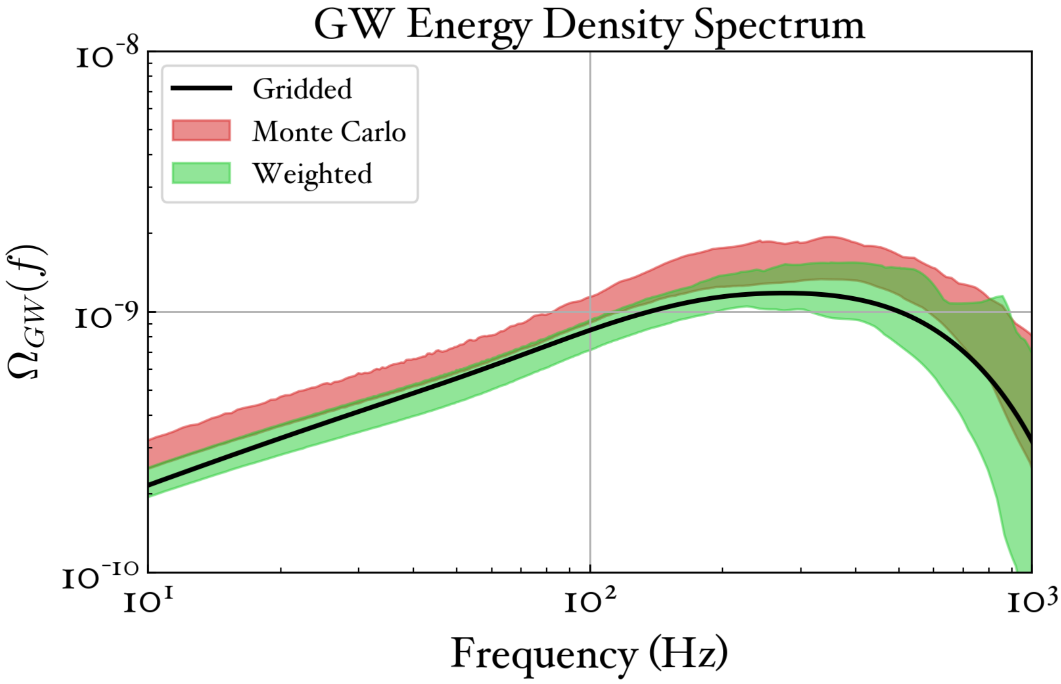

FIGURE 3.1: GW energy density spectra generated by the Gridded, Monte Carlo, and Weighted methods. Highlighted regions bound the 5th and 95th percentiles.

3.1.1 Effect of Maximum Black Hole Mass on the SGWB

In order to investigate how the maximum black hole mass affects the SGWB, five different maximum masses are inserted into the Gridded Method. The chosen masses include the lower bound (38.90 $M_\odot$), average (44.00 $M_\odot$), and upper bound (53.20 $M_\odot$) of the maximum BH mass given by Abbott et al. (2023). The remaining two masses, 41.45 $M_\odot$ and 48.60 $M_\odot$ average the two surrounding values to provide a representative spread of maximum masses.

Figure 3.5 demonstrates that increasing $m_{\rm max}$ is associated with a greater energy density and a lower-frequency peak, which is consistent with the well-documented relation that higher mass systems merge at lower frequencies.

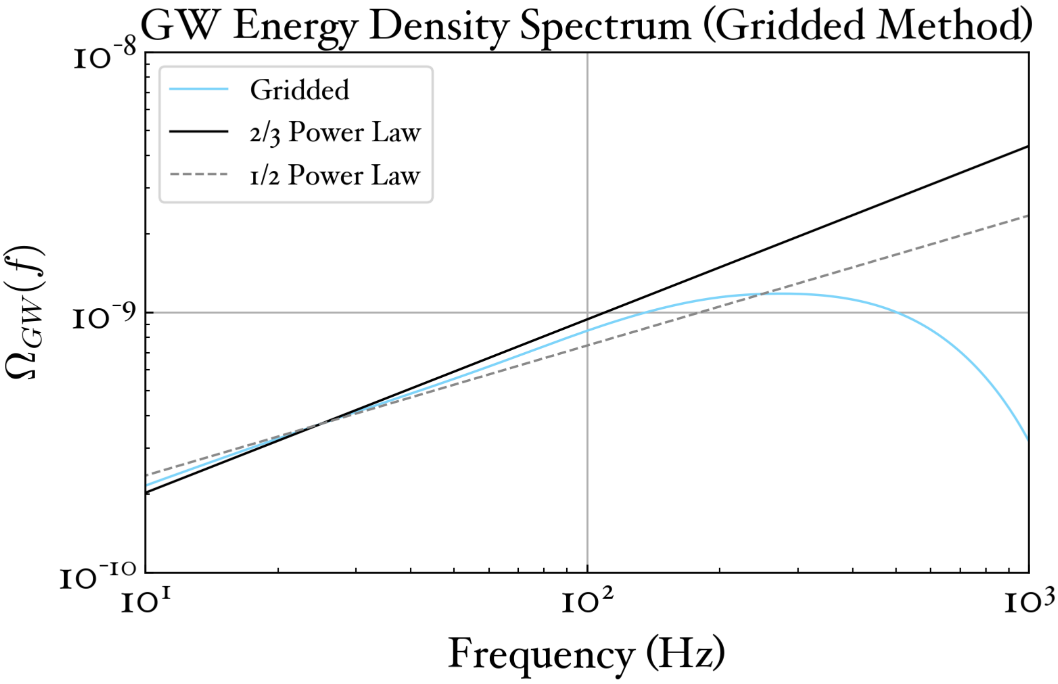

FIGURE 3.2: Predicted SGWB using the Gridded Method.

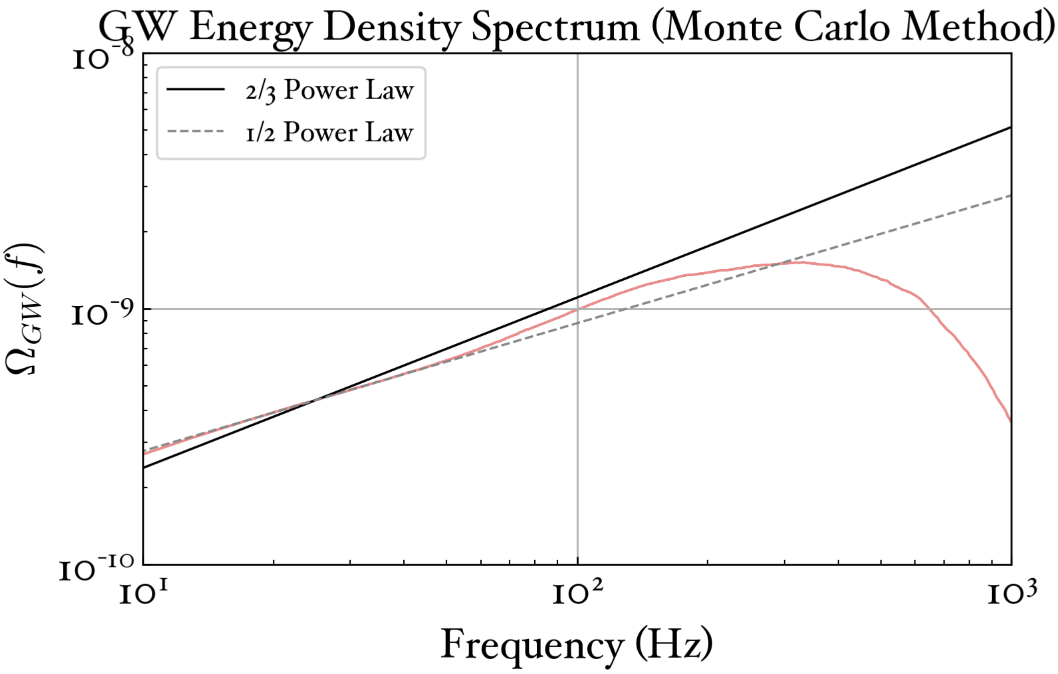

FIGURE 3.3: Predicted SGWB using the Monte Carlo Method using the 50th percentile.

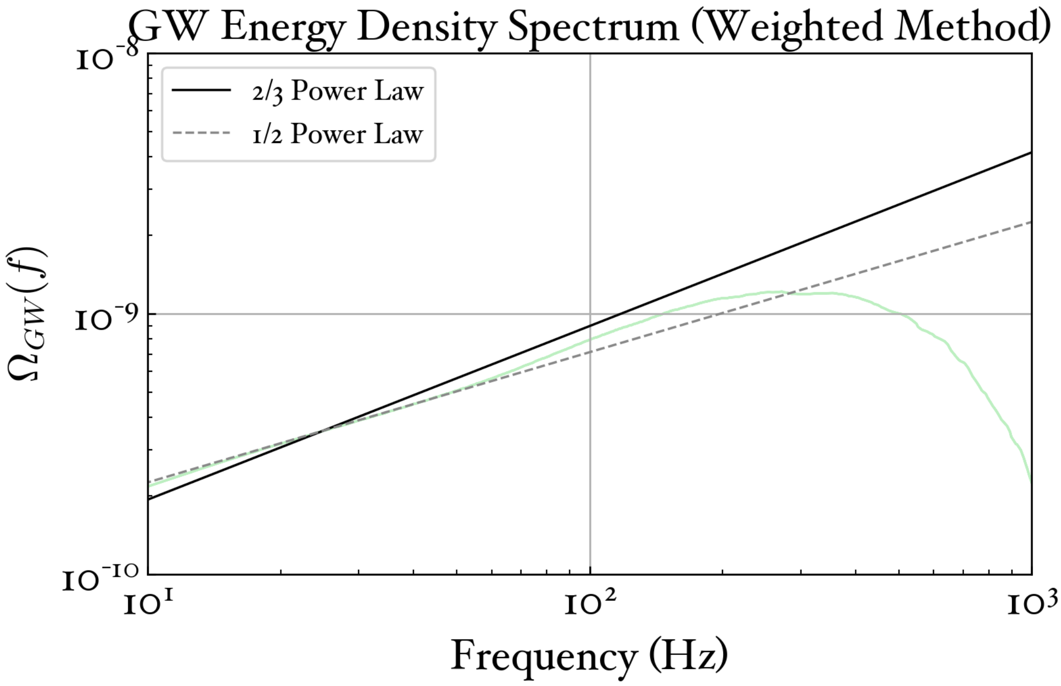

Figure 3.4: Predicted SGWB using the Weighted Method using the 50th percentile.

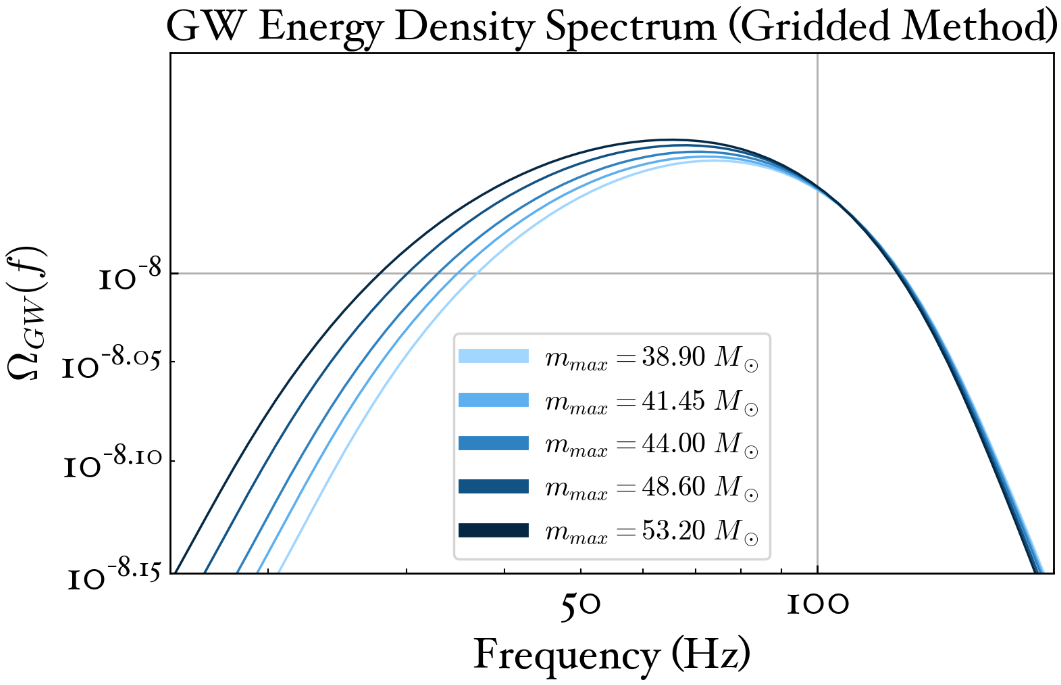

Figure 3.5: GW energy density spectra generated by the Gridded method for varying maximum black hole masses.

3.2 Effect of Merger Rate Parameters on the SGWB

The effect of merger rate parameters on the SGWB is determined by individually varying each of the four merger rate parameters (see Equation 2.7). Figure 3.6 depicts the merger rates that were inserted into the Gridded Method. The values for α and $z_{\rm p}$ are chosen from the bounds given by Callister et al. (2020), while the values for $\mathcal{R}_0$ are based on Abbott et al. (2023). The values for β are chosen arbitrarily, as β immeasurable with current detectors.

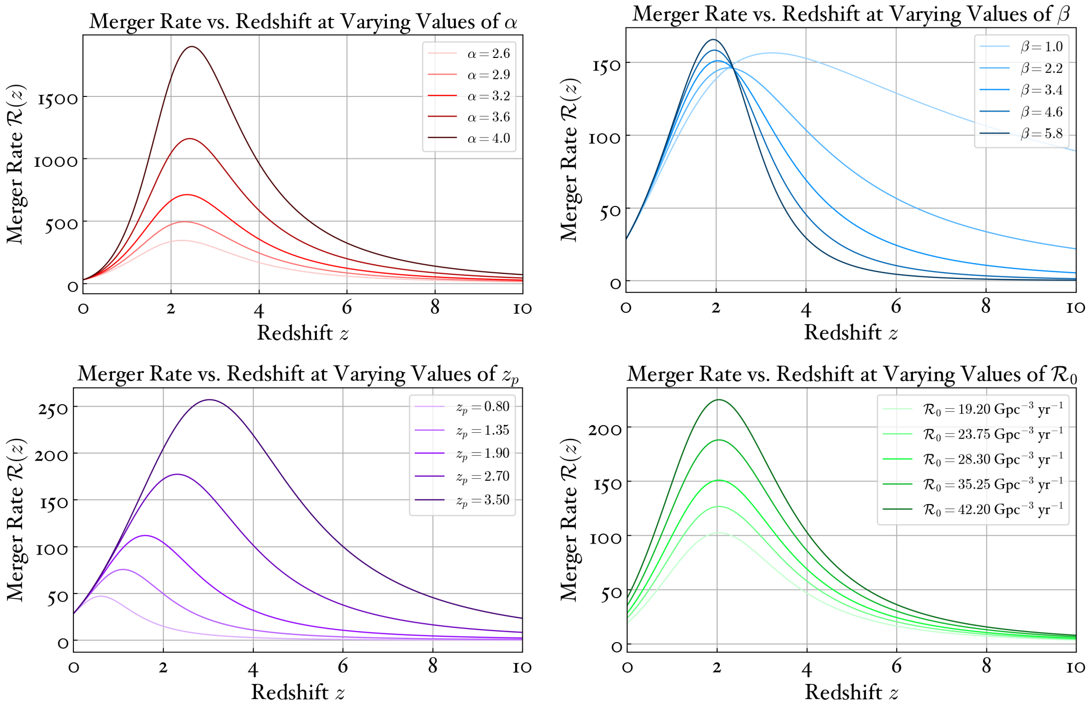

FIGURE 3.6: Merger rate generated for varying values of α, β, $z_{\rm p}$, and $\mathcal{R}_0$ individually.

The value of α affects the merger rate the most notably, especially as $\mathcal{R}(z_{\rm peak})$ ranges from approximately 350 Gpc $^{-3}$ yr^{-1} to 1900 Gpc $^{-3}$ yr^{-1}. Increasing values of α are associated with larger merger rate amplitudes, a shift of the peak to higher redshifts, and a noticeable narrowing of the peak.

Increasing values of β shift the merger rate peak to lower redshifts and higher amplitudes after a certain threshold. For $\beta = 1.0$, the different behavior occurs because β is much less than α. Large values of β also cause significant narrowing of $\mathcal{R}(z)$.

The value of z_p directly controls the redshift of the peak. In addition, increasing z_p produces increased amplitudes.

The local merger rate $\mathcal{R}_0$ is directly proportional to the merger rate, meaning that $c\mathcal{R}_0$ produces a merger rate of $c\mathcal{R}(z)$, where c is an arbitrary constant. The variation in the merger rate is significantly greater for α than the other parameters. Even small changes in α can drastically affect the merger rate.

The merger rates depicted in Figure 3.6 are inserted into the Gridded Method. The resulting spectra are shown in Figure 3.7. The parameters α and $\mathcal{R}_0$ have the greatest impact on the energy density spectrum. Increasing values of α increase the amplitude of Ω_GW and shift the peak to lower frequencies, in contrast to the merger rate.

Both β and z_p do not significantly affect the SGWB. One notable feature, though is that increasing β and z_p results in closer spacing between adjacent peaks. In other words, the distance between the peaks decreases as β and z_p increase.

$\mathcal{R}(z)$ can be taken out of the integral in Equation 2.1 and as a result, linearly scales Ω_GW.

For all four parameters, the spread of amplitudes for low frequencies is much higher than for high frequencies, leading to the conclusion that the merger rate parameters primarily affect low frequencies.

3.3 Effect of Spin on the SGWB

Eight different spin distributions were used to study the effect of spin on the SGWB (see Table 3.1). The values a and $\cos(\theta)$ refer to the spin magnitude and cosine of the tilt angle, respectively.

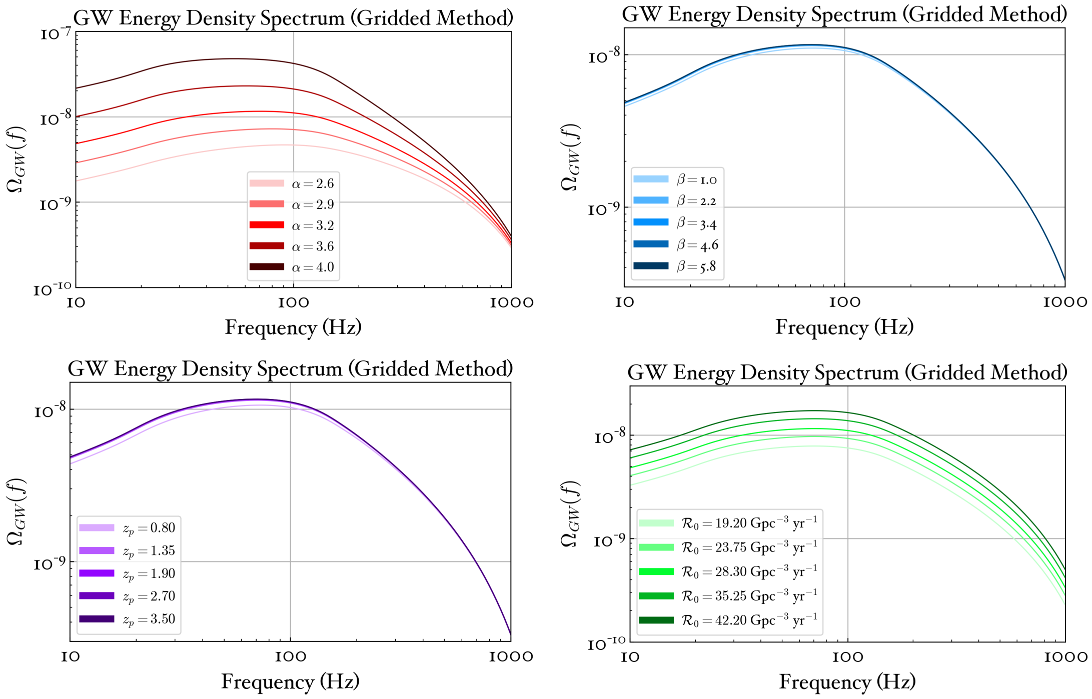

FIGURE 3.7: GW energy density spectra generated by the Gridded method for varying values of α, β, z_{p}, and $\mathcal{R}_0$.

#	a		$\cos(\theta)$	
	Prior	Hyperparameters	Prior	Hyperparameters
1	Isotropic	1	Isotropic	1
2	Isotropic	1	Isotropic	-1
3	Truncated Gaussian	$\mu = 1$, $\sigma = 0.5$	Isotropic	1
4	Truncated Gaussian	$\mu = 1$, $\sigma = 0.5$	Isotropic	-1
5	Truncated Gaussian	$\mu = 0$, $\sigma = 0.5$	Isotropic	1
6	Truncated Gaussian	$\mu = 0$, $\sigma = 0.5$	Isotropic	-1
7	None	0	None	
8	Uniform	min $= 0$, max $= 1$	Uniform	min $= 0$, max $= \pi$

TABLE 3.1: List of different spin distributions that use different priors, spin magnitudes, and tilt angles. The parameter a is the spin magnitude, and θ is the tilt angle of the BBH. We refer to 1 as High Aligned, 2 as High Anti-Aligned, 3 as High Truncated Aligned, 4 as High Truncated Anti-Aligned, 5 as Low Truncated Aligned, 6 as Low Truncated Anti-Aligned, 7 as None, and 8 as Uniform.

The Monte Carlo Method with priors outlined by Table 2.1 was used to calculate the energy density for each distribution. The injection list was kept constant except for component spin magnitudes and tilt angles in order to ensure that

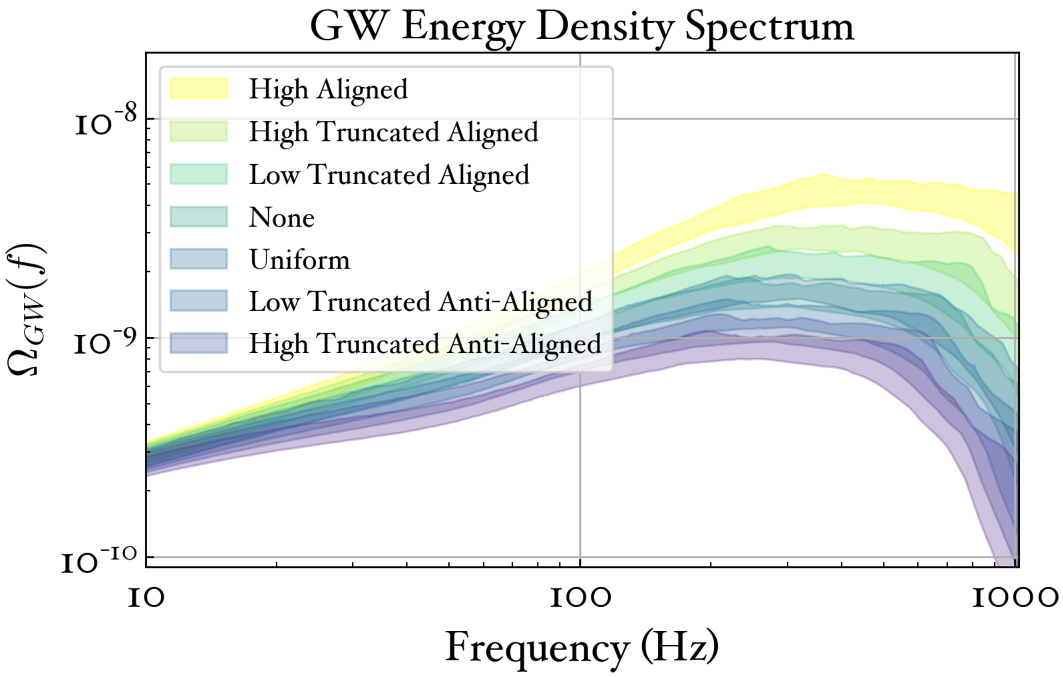

FIGURE 3.8: Predicted Ω_{GW} for various spin distributions.

spin was the only changing parameter. The 5th and 95th percentiles of each distribution are shown in Figure 3.8. The peak GW energy density varies nearly an order of magnitude between the different spin distributions, even considering statistical errors in calculation and uncertainty in BBH population parameters. The High Aligned distribution (Isotropic with $a = 1$ and $\cos(\theta) = 1$) produces the SGWB with the greatest amplitude, while the High Anti-Aligned distribution (Isotropic with $a = 1$ and $\cos(\theta) = -1$) has the lowest amplitude. The High Truncated Aligned and Anti-Aligned distributions have the second greatest and second lowest GW energy density peaks, respectively. The Low Truncated Aligned and Anti-Aligned have the third greatest and third lowest peaks. The GW energy densities of the Uniform distribution and the absence of spin fall in the middle of the range. Therefore, the spread of output GW energy densities follows a symmetrical pattern, suggesting that we can use a measured SGWB to predict the spin distribution of BBHs.

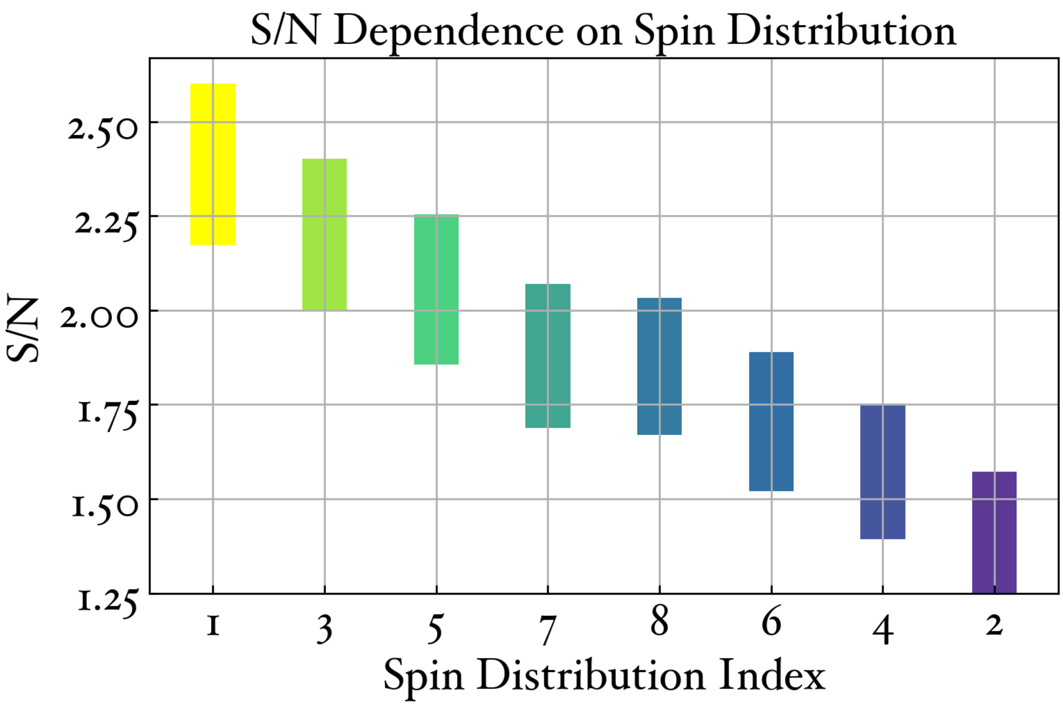

FIGURE 3.9: Signal to noise ratio for the spin distributions listed in Table 3.1 assuming one year of observation time. The upper and lower bounds for each distribution are the 5th and 95th percentiles.

3.3.1 Signal to Noise Ratio

We also investigate the impact of spin distribution on the signal to noise ratio (SNR) for the SGWB. The SNR can be calculated by dividing the optimal estimator of the stochastic background $\hat{\Omega}_{\mathrm{r},\alpha}$ by the inverse standard deviation of the estimator $\sigma_{\mathrm{r},\alpha}$:

$$\mathrm{SNR}_\alpha = \frac{\hat{\Omega}_{\mathrm{r},\alpha}}{\sigma_{\mathrm{r},\alpha}}, \tag{3.1}$$

where α is the spectral index. See Romano & Cornish (2017) for a more detailed description and derivation.

Figure 3.9 depicts the SNR for each of the eight spin distributions in Table 3.1 for one year of observation time without accounting for signal noise. The SNR for different spin distributions follows the same symmetric pattern as the corresponding SGWB predictions. The High Aligned distribution has the greatest SNR, the High Anti-Aligned the lowest, and the pattern continues. As a result, the SNR of

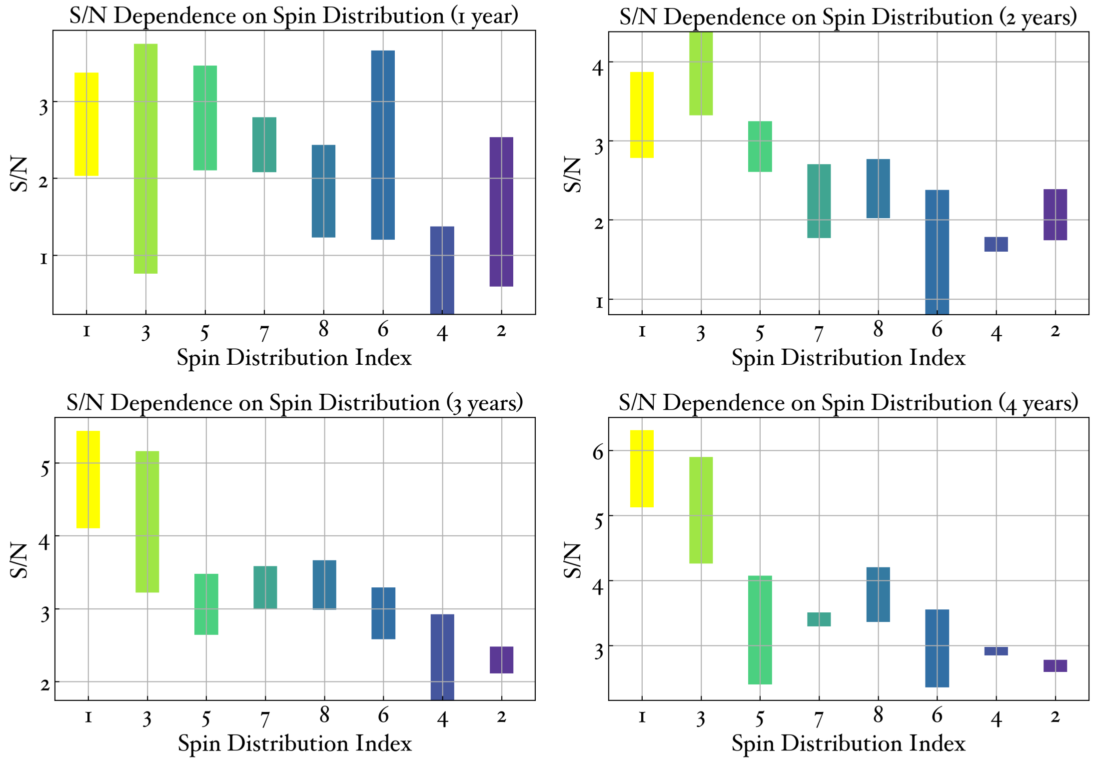

FIGURE 3.10: SNR dependence on spin distribution with varying observation times.

a future SGWB detection may also provide insight into the BBH spin distribution.

Assuming that future detector data will be noisy, the SNR becomes quite unstable and uncertain due to the low amplitude of the SGWB compared to the detector noise. For example, Figure 3.10 shows the SNR for Distribution 5 using an observation time of three years (lower left panel) to be anywhere between approximately 2 and 6. The detector noise is assumed to be consistent with A+ LIGO design. However, Figure 3.10 also demonstrates that longer observation times result in higher SNR, as expected. As a result, with more sensitive detectors in the future and longer observation times, we may still be able to use the SNR to constrain the BBH spin distribution.

CHAPTER 4: Conclusion

There are numerous directions for future work. For example, we could produce a more in-depth analysis of the 2/3 power law deviation and the high frequency peak exhibited by the Monte Carlo Method. In addition, a more nuanced examination of spin distributions could provide a numerical relation between GW energy density peak, spin magnitude, and tilt angle.

We have already begun investigating more realistic spin distributions, such as the one used in Callister & Farr (2023). The spin magnitude model follows a Truncated Lorentzian with $\gamma = 0.18$, $\chi_0 = 0.15$:

$$p(\chi) = \frac{\mathcal{C}}{\gamma}\left[1 + \left(\frac{\chi - \chi_0}{\gamma}\right)^2\right]^{-1}, \tag{4.1}$$

$$\mathcal{C} = \left[\tan^{-1}\left(\frac{1-\chi_0}{\gamma}\right) + \tan^{-1}\left(\frac{\chi_0}{\gamma}\right)\right]^{-1}, \tag{4.2}$$

$$\tag{4.3}$$

where $\gamma = 0.18$, $\chi_0 = 0.15$, and $\mathcal{C}$ is a normalization constant. The tilt angle model follows an Isotropic/Gaussian in $\cos(\theta)$ with $\mu = 0.59$ and $\sigma = 0.58$:

$$p(\cos\theta) = \frac{f_{\mathrm{iso}}}{2} + (1 - f_{\mathrm{iso}})N_{[-1,1]}(cos\theta|\mu,\sigma), \tag{4.4}$$

where $f_{\mathrm{iso}} = 0.67$ is the isotropic fraction and $N_{[-1,1]}$ is a truncated Gaussian on $-1 \leq \cos\theta \leq 1$ with $\mu = 0.59$ and $\sigma = 0.58$. Instead of using `bilby` priors, sampling for the Callister/Farr Distribution is performed using rejection sampling (see Appendix C).

In this study, however, we implement and compare three different methods to calculate the stochastic gravitational-wave background. We find that deviations from the assumed 2/3 power law in the output gravitational-wave energy density using the Monte Carlo Method reveals complexities in the inspiral phase for binary black holes due to high mass systems. We also analyze the effect of maximum black hole mass, merger rate parameters, and spin distribution on the SGWB.

Increasing maximum black hole mass produces a GW energy density peak greater in amplitude and lower in frequency. In addition, merger rate parameters primarily affect frequencies less than z_{p}, the redshift at which the merger rate is at a maximum. Finally, we conclude that the spin distribution has a significant effect on the SGWB, with greater spin magnitudes associated with a shift in the GW energy density peak to greater amplitudes and frequencies.

APPENDIX A: Hubble Rate

The Hubble parameter is a measure of the expansion of the universe in units of km s^{-1} Mpc^{-1}:

$$H(z) = H_0(\Omega_{\rm R}(1+z)^4 + \Omega_{\rm M}(1+z)^3 + \Omega_{\rm k}(1+z)^2 + \Omega_\Lambda)^{1/2}, \tag{A.1}$$

$$\Omega_{\rm R} = \Omega_\gamma + \Omega_\nu + \Omega_{\rm GW} + ..., \tag{A.2}$$

where $H(z)$ is the Hubble parameter, H_0 is the current Hubble parameter ($z = 0$), z is redshift, and Ω is the energy density with R as the radiation component, M as the matter component, k as the curvature, and Λ as the cosmological constant, representative of dark energy. R is composed of photons, neutrinos, and GWs, while M is composed of baryons and cold dark matter. According to the Planck 2018 cosmological parameters, $H_0 = 67.66 \pm 0.42$ km s^{-1} Mpc^{-1}, $\Omega_{\rm R} = 9.182 \times 10^{-5}$, $\Omega_{\rm M} = 0.3111 \pm 0.0056$, $\Omega_{\rm k} = 0.001 \pm 0.002$, and $\Omega_\Lambda = 0.6889 \pm 0.0056$ (Aghanim et al. 2020).

The quantity $\Omega_{\rm R}$ is particularly notable at high redshift, which is concurrent with the radiation-dominated era of the cosmological timeline, suggesting that $\Omega_{\rm GW}$ becomes a measurable quantity when probing the early Universe.

APPENDIX B: Poisson Process

A Poisson process is a method used for weighted sampling and is defined by the following equation:

$$p(n) = \frac{(\lambda t)^n}{n!} e^{-\lambda t}. \tag{B.1}$$

In the context of the SGWB, p is the probability that n events occurs in an observing time t and λ is the total merger rate. Therefore, λt is equivalent to N in Equation 2.19. Equation B.1 then represents a probability distribution from which to draw the number of injections.

APPENDIX C: Rejection Sampling

Rejection sampling is a simple but effective algorithm that draws N samples of a parameter θ from a specified probability distribution $p(\theta)$. The algorithm begins by initializing a list of samples S. A random sample (θ_0, p_0) is then generated such that $\theta_{\min} \leq \theta_0 \leq \theta_{\max}$ and $p_{\min}(\theta) \leq p_0 \leq p_{\max}(\theta)$. If $p_0 > p(\theta_0)$, then θ_0 is accepted and added to S. Otherwise, θ_0 is rejected. The process of generating random samples repeats until the number of accepted samples is equal to N.

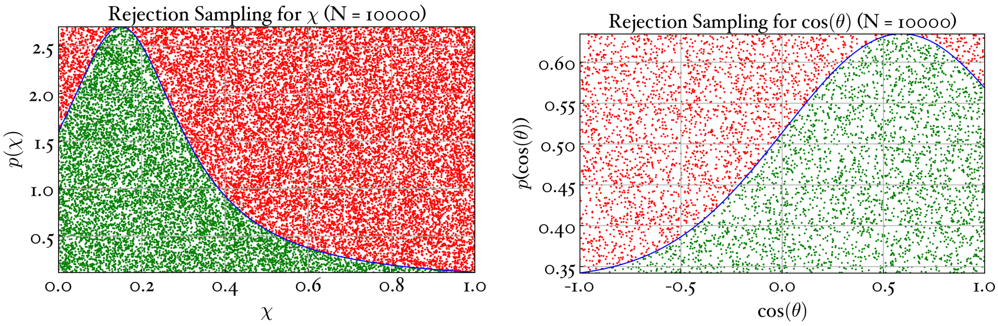

FIGURE C.1: Priors for χ and cosθ with rejection sampling.

To illustrate the algorithm visually, consider the spin and cosθ priors defined by Callister & Farr (2023) (see Equations 4.1 and 4.4). We take $-1 \leq \chi \leq 1$ as the spin magnitude of a black hole and $-1 \leq \cos\theta \leq 1$ as the cosine of the tilt angle.

Figure C.1 demonstrates that random sampling of θ and $p(\cos\theta)$ results in a uniform distribution of points over $(p(\theta), \theta)$ space. In order to choose a subset of points that fits the desired distribution, we select points that lie under $p(\theta)$. As a result, the red points are rejected, while the green points are accepted. Since each infinitesimal width $d\theta$ is associated with a different height $p(\theta)$, the probability of a random point landing under the curve varies with $p(\theta)$, and the algorithm successfully samples N parameters that follow distribution $p(\theta)$.

APPENDIX C: Bibliography

Aasi, J., et al. 2015, Class. Quant. Grav., 32, 074001, doi: 10.1088/0264-9381/32/7/074001

Abbott, B. P., Abbott, R., Abbott, T. D., et al. 2016, Phys. Rev. Lett., 116, 061102, doi: 10.1103/PhysRevLett.116.061102

—. 2017, Classical and Quantum Gravity, 34, 044001, doi: 10.1088/1361-6382/aa51f4

—. 2019, The Astrophysical Journal, 886, 75, doi: 10.3847/1538-4357/ab4b48

—. 2020, Living Reviews in Relativity, 23, doi: 10.1007/s41114-020-00026-9

Abbott, R., Abbott, T. D., Abraham, S., et al. 2021, Phys. Rev. D, 104, 022004, doi: 10.1103/PhysRevD.104.022004

Abbott, R., Abbott, T. D., Acernese, F., et al. 2023, Physical Review X, 13, 011048, doi: 10.1103/PhysRevX.13.011048

Abbott, R., Abbott, T. D., Acernese, F., et al. 2023, Phys. Rev. X, 13, 011048, doi: 10.1103/PhysRevX.13.011048

Acernese, F., et al. 2015, Class. Quant. Grav., 32, 024001, doi: 10.1088/0264-9381/32/2/024001

Affeldt, C., Danzmann, K., Dooley, K. L., et al. 2014, Classical and Quantum Gravity, 31, 224002, doi: 10.1088/0264-9381/31/22/224002

Agazie, G., Anumarlapudi, A., Archibald, A. M., et al. 2023, The Astrophysical Journal Letters, 951, L8, doi: 10.3847/2041-8213/acdac6

Aghanim, N., Akrami, Y., Ashdown, M., et al. 2020, Astronomy &amp Astrophysics, 641, A6, doi: 10.1051/0004-6361/201833910

Ajith, P., Babak, S., Chen, Y., et al. 2008, Phys. Rev. D, 77, 104017, doi: 10.1103/PhysRevD.77.104017

Akutsu, T., Ando, M., Arai, K., et al. 2020, Progress of Theoretical and Experimental Physics, 2021, 05A101, doi: 10.1093/ptep/ptaa125

Ashton, G., Hübner, M., Lasky, P. D., et al. 2019, ApJS, 241, 27, doi: 10.3847/1538-4365/ab06fc

Aso, Y., Michimura, Y., Somiya, K., et al. 2013, Phys. Rev. D, 88, 043007, doi: 10.1103/PhysRevD.88.043007

Babak, S., Hewitson, M., & Petiteau, A. 2021, LISA Sensitivity and SNR Calculations. https://arxiv.org/abs/2108.01167

Biscoveanu, S., Isi, M., Varma, V., & Vitale, S. 2021, Physical Review D, 104, doi: 10.1103/physrevd.104.103018

Bustillo, J. C., Evans, C., Clark, J. A., et al. 2020, Communications Physics, 3, doi: 10.1038/s42005-020-00446-7

Callister, T., Fishbach, M., Holz, D. E., & Farr, W. M. 2020, The Astrophysical Journal Letters, 896, L32, doi: 10.3847/2041-8213/ab9743

Callister, T., Sammut, L., Qiu, S., Mandel, I., & Thrane, E. 2016, Phys. Rev. X, 6, 031018, doi: 10.1103/PhysRevX.6.031018

Callister, T. A. 2021, A Thesaurus for Common Priors in Gravitational-Wave Astronomy. https://arxiv.org/abs/2104.09508

Callister, T. A., & Farr, W. M. 2023, A Parameter-Free Tour of the Binary Black Hole Population. https://arxiv.org/abs/2302.07289

Dooley, K. L., Leong, J. R., Adams, T., et al. 2016, Classical and Quantum Gravity, 33, 075009, doi: 10.1088/0264-9381/33/7/075009

EPTA Collaboration, InPTA Collaboration, Antoniadis, J., et al. 2023, A&A, 678, A50, doi: 10.1051/0004-6361/202346844

Evans, M., Adhikari, R. X., Afle, C., et al. 2021, A Horizon Study for Cosmic Explorer: Science, Observatories, and Community. https://arxiv.org/abs/2109.09882

Hild, S., Abernathy, M., Acernese, F., et al. 2011, Classical and Quantum Gravity, 28, 094013, doi: 10.1088/0264-9381/28/9/094013

Khan, S., Chatziioannou, K., Hannam, M., & Ohme, F. 2019, Phys. Rev. D, 100, 024059, doi: 10.1103/PhysRevD.100.024059

Luck, H., et al. 2010, J. Phys. Conf. Ser., 228, 012012, doi: 10.1088/1742-6596/228/1/012012

Martynov, D. V., Hall, E. D., Abbott, B. P., et al. 2016, Phys. Rev. D, 93, 112004, doi: 10.1103/PhysRevD.93.112004

Piccinni, O. J. 2022, Galaxies, 10, doi: 10.3390/galaxies10030072

Punturo, M., Abernathy, M., Acernese, F., et al. 2010, Classical and Quantum Gravity, 27, 084007, doi: 10.1088/0264-9381/27/8/084007

Reardon, D. J., Zic, A., Shannon, R. M., et al. 2023, ApJ, 951, L6, doi: 10.3847/2041-8213/acdd02

Reitze, D., Adhikari, R. X., Ballmer, S., et al. 2019, Cosmic Explorer: The U.S. Contribution to Gravitational-Wave Astronomy beyond LIGO. https://arxiv.org/abs/1907.04833

Renzini, A. I., Goncharov, B., Jenkins, A. C., & Meyers, P. M. 2022, Galaxies, 10, doi: 10.3390/galaxies10010034

Renzini, A. I., Romero-Rodríguez, A., Talbot, C., et al. 2023, The Astrophysical Journal, 952, 25, doi: 10.3847/1538-4357/acd775

Romano, J. D., & Cornish, N. J. 2017, Living Reviews in Relativity, 20, 2, doi: 10.1007/s41114-017-0004-1

Somiya, K. 2012, Classical and Quantum Gravity, 29, 124007, doi: 10.1088/0264-9381/29/12/124007

Team, E. S. 2020, Einstein gravitational wave Telescope conceptual design study, Zenodo, doi: 10.5281/zenodo.3911261

Thrane, E., & Romano, J. D. 2013, Phys. Rev. D, 88, 124032, doi: 10.1103/PhysRevD.88.124032

Turbang, K., Lalleman, M., Callister, T. A., & van Remortel, N. 2023, arXiv e-prints, arXiv:2310.17625, doi: 10.48550/arXiv.2310.17625

Xu, H., Chen, S., Guo, Y., et al. 2023, Research in Astronomy and Astrophysics, 23, 075024, doi: 10.1088/1674-4527/acdfa5